A scheme to correct the influence of calibration misalignment for cross-wire probes in turbulent shear flows

Rahul Deshpande[1] · **Jason P. Monty**[1] · **Ivan Marusic**[1]

Abstract

Velocity fluctuations, measured via multi-wire probes, are very sensitive to misalignment between the calibration coordinate system and that of the wind tunnel. The present study proposes a scheme to correct the erroneous velocity fluctuations processed from a misaligned calibration while investigating a wall-bounded turbulent shear flow. The scheme is based on the premise that the viscous-scaled spectral energy distribution in the small-scales is invariant with Reynolds number and solely depends on the viscous-scaled spatial resolution of the sensor. Energy spectra processed from the misaligned calibration, in this small-scale range, are compared with the 'expected' spectra obtained via synthetic experiments on a direct numerical simulation data set. The erroneous lateral velocity spectra is found to be either relatively amplified or attenuated, by almost the same factor, at all wall-normal distances across the shear flow. A unique gain, defined to be the correction ratio, is thus obtained by forcing the erroneous spectra onto the reference spectra in this scale range. This ratio is further used to rectify the time series of the lateral velocity fluctuations, acquired across the shear flow, via Fourier analysis. The scheme is shown to be effective for experiments conducted across a decade of Reynolds number and using probes of varying spatial resolution.

✉ Rahul Deshpande
raadeshpande@gmail.com

[1] Department of Mechanical Engineering, University of Melbourne, Parkville, VIC 3010, Australia

Published online: 02 March 2020

Graphic abstract

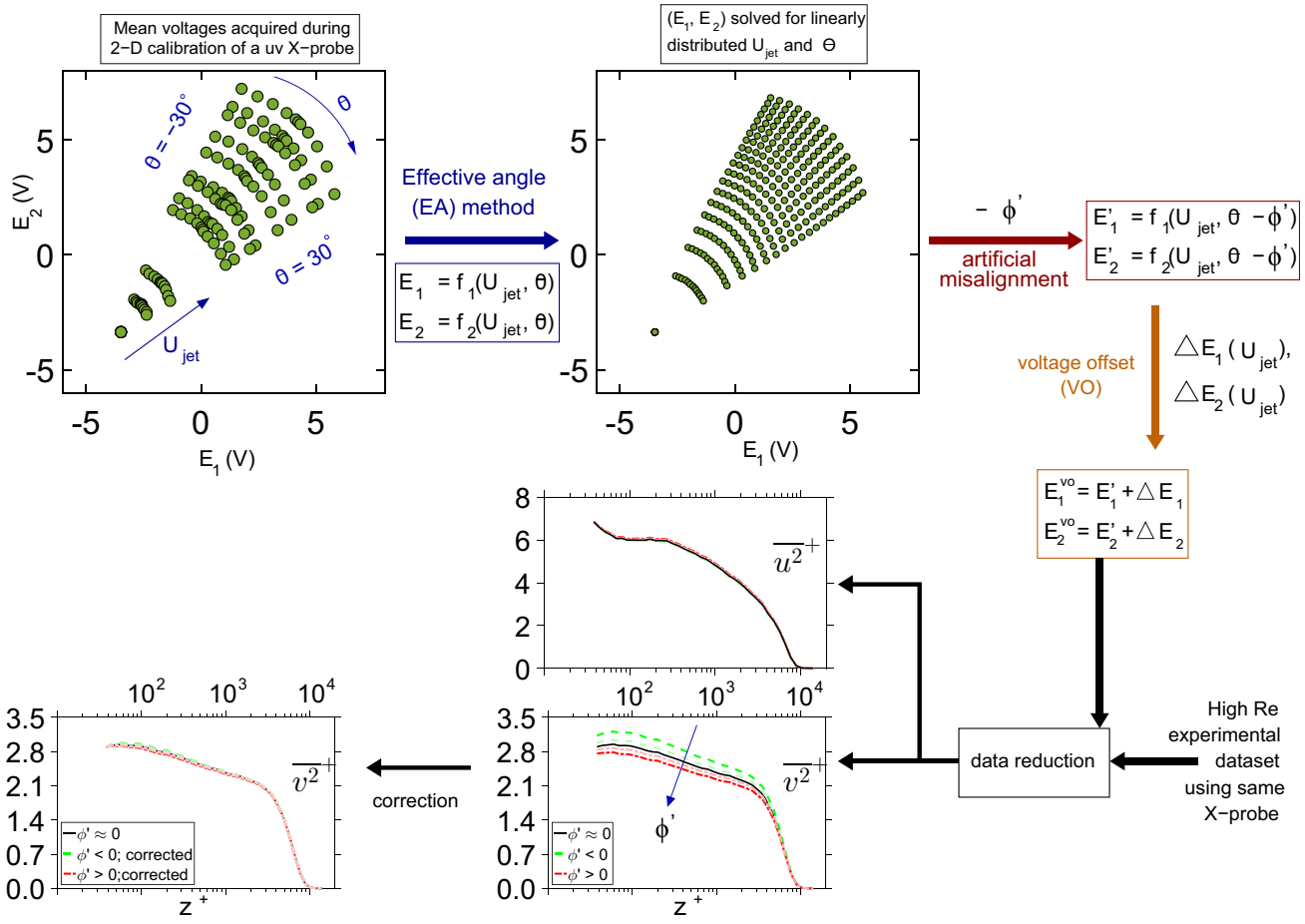

1 Introduction

Development of a variety of multi-wire probes over the last 3 decades has allowed for a deeper investigation into the high Reynolds number dynamics of wall-bounded turbulence (Wallace and Vukoslavčević 2010). Multi-wire probes are highly complex instruments, however, and are prone to error from a range of sources. For example, errors due to the inadequate spatial resolution of these probes, owing to the size of their measuring volumes, have been recognized and investigated previously (Strohl and Comte-Bellot 1973; Browne et al. 1988; Suzuki and Kasagi 1992; Burattini 2008). Availability of direct numerical simulation (DNS) flow fields has allowed researchers (Burattini et al. 2007; Philip et al. 2013; Baidya et al. 2019b; Zimmerman et al. 2017) to perform synthetic experiments and explain these spatially attenuated statistics, in turn inspiring the development of miniature probes (Baidya et al. 2012; Zimmerman et al. 2017). Apart from the issue of spatial resolution, uncertainties in the probe calibration procedure also bring in additional errors and these have been investigated to a limited extent in the literature (Yavuzkurt 1984; Jørgensen 1996). Given the uniqueness of each hotwire sensor in terms of its response (voltage) to the surrounding flow (velocity), calibration of each sensor is critical to determine its velocity–voltage mapping. For a multi-wire probe, the calibration is typically carried out by placing the probe in front of an articulating jet with the capability of varying the flow speed and the incident flow angle. This practise is hence referred as a two-dimensional (2-D) calibration and provides a map between the three velocity components and the corresponding voltages from each sensor.

Jørgensen (1996) found that the lateral velocity fluctuations are more sensitive to the uncertainties in the 2-D calibration than the streamwise velocity fluctuations. Recently, Baidya et al. (2019a) have utilized channel DNS flow fields to investigate the sensitivity of the turbulent stresses to various uncertainties in the calibration procedure for a

cross-wire probe (henceforth referred as an X-probe). One of the uncertainties investigated was the misalignment of a 2-D calibration. A 2-D calibration is said to be misaligned when the coordinate system of the jet does not align with the coordinate system of the wind tunnel. Figure 1 explains this for the case of a *uv* X-probe with x, y and z denoting the streamwise, spanwise and wall-normal directions, respectively, with u, v and w denoting the velocities corresponding to these directions (this convention is followed throughout the manuscript). For the probe shown in Fig. 1, angles ϕ' and ψ' denote the misalignment in the sensor plane and out of the sensor plane, respectively (Fig. 1). Baidya et al. (2019a), through synthetic experiment, showed that all the turbulence stresses are adversely affected by the misalignment, especially the Reynolds shear stress ($\overline{uw}$). Further, they proposed that the angular misalignment for 2-D calibration can be accounted for by rotating the jet reference plane to match a reference 'zero-angle' calibration performed in the wind tunnel, an idea also implemented by Zimmerman et al. (2017). However, this practise of accounting for the misalignment was found to be effective for angular offsets only within ϕ', $\psi' \approx \pm 0.5°$, which is the accuracy level obtained when the jet calibrator is aligned using typical reference devices (eg., laser sheets; refer Sect. 2.1.3).

The problem becomes serious when there are no references available to aid the alignment procedure. Such a situation may be encountered when the probes are not calibrated in situ, i.e., they need to be unmounted from the tunnel traverse to be calibrated at a different location. In situ calibration of a multi-wire probe, which is to be used for measurement in an internal flow geometry (eg., channel, pipe flow), is also challenging given that the jet calibrator cannot be taken inside the working section due to physical constraints (in a majority of cases). The angular offset (ϕ', ψ'), which signifies the degree of misalignment in the 2-D calibration, can be greater than 2° (shown later) in such cases and hence cannot be accounted for by using the methodology implemented by Baidya et al. (2019a), which is applicable only for very small offsets where a linear response of the sensor (with flow angle) may be assumed. In the present study, we encountered a similar scenario while attempting to conduct velocity profile measurements using an X-probe in a channel flow facility (refer Sect. 2.1.1). Here, we attempt to highlight the effect of such a calibration misalignment on the velocity statistics and spectra, followed by proposal of a scheme to correct the erroneous velocity fluctuations using synthetic experiments as a reference. Throughout this article, capitalization and over-bars indicate time-averaged quantities, while superscript '+' denotes normalization by viscous units (eg., $U^+ = U/U_\tau$ and $z^+ = zU_\tau/\nu$, where U_τ and ν correspond to the mean friction velocity and kinematic viscosity, respectively).

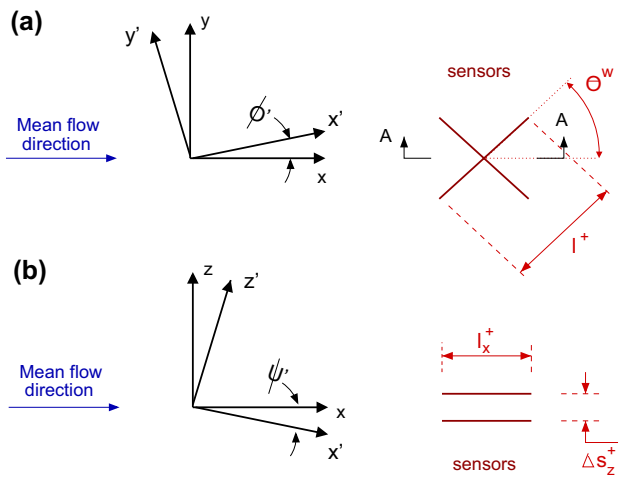

Fig. 1 A schematic representation of the misalignment between the wind-tunnel coordinate system (x–y–z) and the coordinate system for the 2-D jet calibrator (x'–y'–z') for an X-probe oriented to measure the u and v velocities. Sensors are represented by solid lines in red. The angles **a** ϕ' and **b** ψ' correspond to the in-plane and out-of-plane misalignment with reference to the sensor plane (which is x–y for the *uv* X-probe), respectively. Also highlighted is the sensor length (l^+), spacing between the two sensors (Δs^+) and angle (θ^w) made by each sensor with x, with subscripts denoting the direction in which they are measured

2 Experimental setup

Physical experiments have been performed in the channel and boundary layer flow to demonstrate the effect of 2-D calibration misalignment on the velocity statistics. Table 1 gives details of these experiments and the various X-probes used. Synthetic experiments, corresponding to these X-probes, are also performed on DNS flow fields of a turbulent channel flow (del Alamo et al. 2004) and are used as a basis to correct the erroneous statistics.

2.1 Physical experiments

2.1.1 Flow facilities

Physical experiments were conducted in the channel flow facility and the high Reynolds number boundary layer wind tunnel (HRNBLWT) housed in the University of Melbourne. Each of these is a blowdown type non-recirculating wind tunnel with the inlet flow tripped via sandpaper strips to ensure a fully turbulent flow at the X-probe measuring station. During zero pressure gradient turbulent boundary layer (ZPG TBL) measurements, the free-stream speed of the tunnel was maintained at 15 ms^{-1} and the probe was located at 13 m from the start of the working section, giving a friction Reynolds number, Re_τ ($= U_\tau \delta/\nu$) $\approx$ 10,000 for the

Table 1 A summary of the various physical experiments conducted

Probe	Ref.	Re_τ	Probe type	Flow type	h or δ (in m)	ν/U_τ (in μm)	θ_w (in °)	l_x^+, l_y^+ or l_z^+	Δs_y^+ or Δs_z^+	l/d	Symbol	Misaligned 2-D Cal only
Auspex A55P51	*AX*1	1000	*uv*,*uw*	Channel	0.05	50	45	14	10	200	Green triangle	✓
Auspex A55P61	*AX*2	1000	*uv*,*uw*	Channel	0.05	50	45	7	10	200	Blue inverted triangle	✓
Custom	*CX*	1000	*uv*,*uw*	Channel	0.05	50	45	7	4	200	Red diamond	✓
		10,000	*uv*,*uw*	ZPG TBL	0.32	32	45	12	7	200	Black circle	

Terminology has been described in Sect. 2.1.2. Synthetic experiments were conducted corresponding to the viscous-scaled measuring volume (a function of l^+ and Δs^+) for each case mentioned. Statistics from these synthetic experiments are plotted with the same symbol and a lighter color shade as for the corresponding physical experiments. A checkmark (✓) in the last column refers to experimental cases where all available 2-D calibrations were misaligned, i.e., no 'accurate' 2-D calibration could be conducted

measurement. Both U_τ and δ (boundary layer thickness) were obtained by fitting the mean velocity profile to the composite velocity formulation given by Chauhan et al. (2009). More details regarding HRNBLWT may be found in Baars et al. (2016).

The channel flow experiments were performed in the same facility used by Monty et al. (2007, 2009). The aspect ratio of the channel cross section is 11.7:1 which is sufficient to ensure minimal sidewall influence and the measurement station was located at nearly $410h$ from the beginning of the working section, with h being the channel half-height. The channel centerline speed was maintained at 6.5 ms^{-1} approximately to achieve an $Re_\tau (= U_\tau h/\nu) \approx 1000$, where U_τ is estimated by recording the pressure gradient across the channel working section.

During velocity profile measurements in each facility, the X-probe was traversed across the turbulent shear flow beginning from the position closest to the wall, which was estimated by using a traversable microscope. From thereon, the probe was traversed to logarithmically spaced locations by a linear rail mechanism governed by a *Renishaw* linear encoder with a resolution of 0.5 μm, approximately. Such a resolution allows estimation of z^+ within error margin of $O(10^{-2})$ which, as will be seen ahead, is important for the effectiveness of the correction scheme proposed in this study.

2.1.2 Hotwire sensor and anemometry details

The X-probes listed in Table 1 differ in terms of their viscous-scaled measuring volumes. Here, l_i^+ refers to the length of the sensing element while Δs_i^+ refers to the spacing between the two sensors with subscript i specifying the direction in which it is measured, which depends on type of the probe (*uv* or *uw*) . For example, for a *uv* X-probe (Fig. 1), the measuring volume is given by $l_x^+ \times l_y^+ \times \Delta s_z^+$. θ_w refers to the angle made by both the sensing elements with the free-stream (x) direction and d refers to the diameter of the sensor. Accordingly, the included angle of the X-probe is two times θ^w, which is 90° for all X-probes used in the present study. Since here we are solely dealing with canonical wall-bounded turbulence, an included angle of 90° is deemed sufficient (Tagawa et al. 1992) to avoid errors due to rectification (Tutu and Chevray 1975). This angle should however be greater than 90° for measurements in high turbulence intensity fields such as rough wall flows (Perry et al. 1987) and flows with adverse pressure gradients (APG; Marusic and Perry 1995) in order to avoid the scenario where the erroneous statistics due to rectification are misrepresented as a calibration error, which is being investigated in this study.

Probes *AX*1 and *AX*2 are standard probes purchased from Auspex Corporation, whereas the *CX* probe is manufactured in-house (Baidya et al. 2012) with the aim of minimizing the measuring volume and the associated errors due to spatial resolution. During measurement, the probes were connected to a Dantec 55H25 X-probe holder and operated by an in-house Melbourne University Constant Temperature Anemometer (MUCTA) at an overheat ratio of 1.8. Negligible thermal cross talk was noted between the two hotwire sensors when exposed to the velocity range of interest. A high overheat ratio allowed us to set a system frequency response corresponding to $t^+ < 1.5$ which is sufficient to capture the highest frequency information in a wall-bounded turbulent flow (Hutchins et al. 2009). The hotwire signals were sampled at an interval of $\Delta t^+ \leq 0.6$ for a minimum duration of $15,000\delta/U_\infty$ s, where U_∞ is the mean centerline or free-stream velocity.

2.1.3 Probe calibration and data processing technique

The 2-D calibration of the X-probes was performed with an articulating compressed-air driven jet facility. During calibration, the X-probe was positioned such that the two sensors were in the central 'irrotational' portion of the flow exiting the jet nozzle. The jet was rotated through a series of angles: $-30° < \theta < 30°$ in the sensor plane of the probe,

which is sufficient for calibrating an X-probe (Baidya 2016). Angular encoders positioned along both the rotation axes provided accurate measurement of the change in jet angle relative to an initially declared reference location of $\theta = 0°$. This sweep of the jet angles is repeated for multiple jet velocities (U_{jet}) to record the corresponding voltages from wire 1 and wire 2 (E_1 and E_2) and obtain a one-to-one mapping between the voltage–velocity pairs following: $E_1 = a(U_{jet}, \theta)$ and $E_2 = b(U_{jet}, \theta)$. Figure 2a shows the voltage pairs acquired during a typical 2-D calibration, as an example. Next, the voltages are fitted to smooth functions of jet velocities and angles determined based on the effective angle method (EAM; Bradshaw 2013), giving $E_1 = f_1(U_{jet}, \theta)$ and $E_2 = f_2(U_{jet}, \theta)$. These functions are then solved for a linearly distributed set of U_{jet} and θ to get a voltage map as shown in Fig. 2b. The fitted functions are finally inverted to generate calibration surfaces of the form: $u = f(E_1, E_2)$ and v (or w) $= g(E_1, E_2)$. It is worth mentioning that although the look-up table technique (LUT; Willmarth and Bogar 1977) has been found to be more reliable than EAM (Burattini and Antonia 2005), the latter was preferred in the present study. This is because most LUT schemes do not use theoretical equations but rather rely on a one-to-one voltage pair to velocity relationship obtained from the calibration. Since the measured velocity fluctuations are directly influenced by the gradient of the LUT scheme (Morrill-Winter et al. 2015; Baidya 2016), a fit selected without a theoretical basis has a potential to introduce uncertainties. Since the present study is focused on identifying, as well as correcting, the errors due to calibration misalignment, the intention was to avoid introduction of any further (intractable) errors into the data reduction procedure, and thus EAM was chosen over LUT.

Apart from the 2-D calibration, another calibration (henceforth referred as 1-D calibration) is performed by traversing the X-probe to the free-stream (or centerline in case of the channel) and recording voltages corresponding

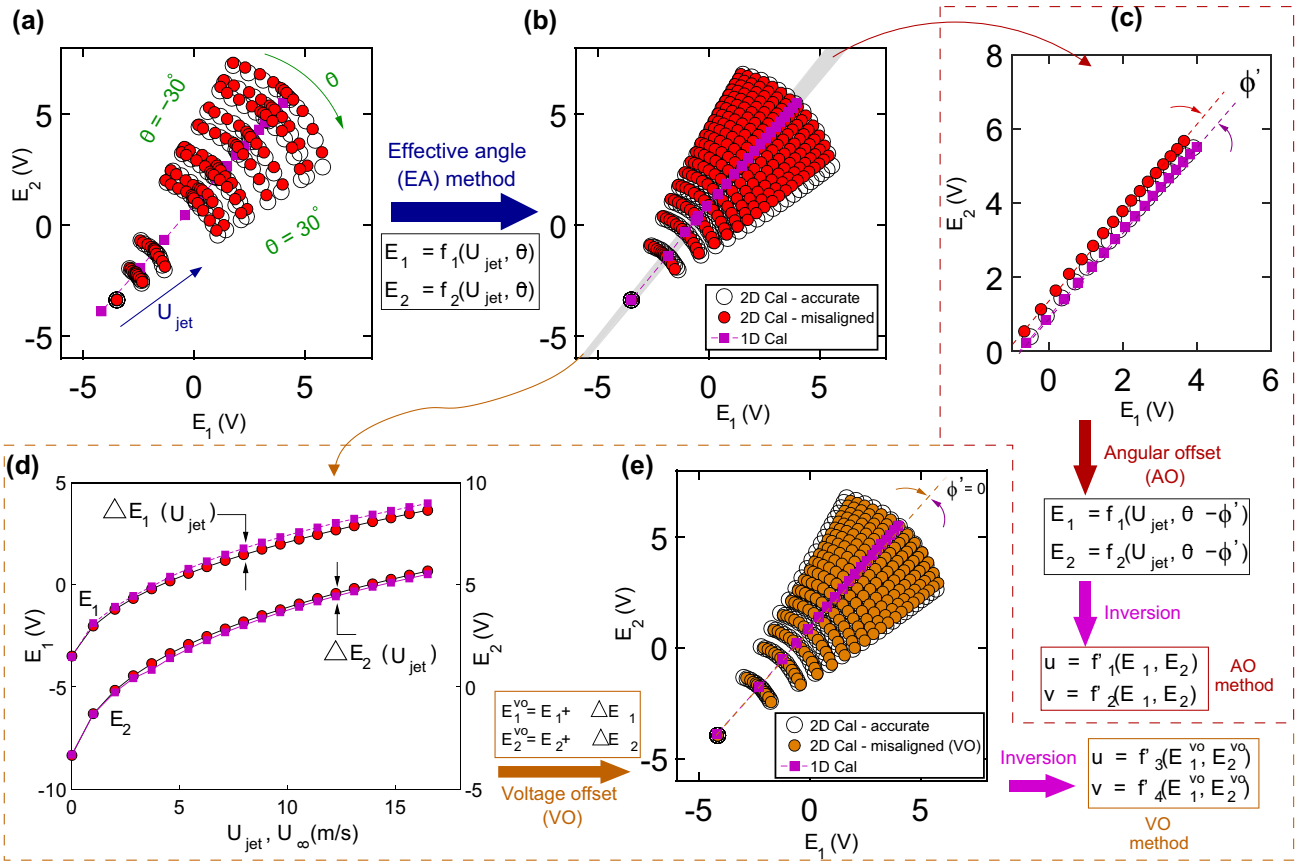

Fig. 2 Procedure to account for misalignment while processing 2-D calibration of a *uv*-CX probe, explained by using an 'accurate' 2-D calibration as a reference: **a** voltage pairs obtained by varying the U_{jet} and θ for an *accurate* and misaligned 2-D calibration along with the voltages obtained from the 1-D calibration in HRNBLWT just before the measurement. **b** Voltages in **a** interpolated onto a linearly distributed set of U_{jet} and θ based on effective angle method. **c** Comparison of 2-D calibration voltage pairs corresponding to $\theta = 0°$ (highlighted by gray background in **b**) with 1-D calibration to obtain the angular offset ϕ'. **d** The same voltage pairs as in **c**, but compared individually for the two sensors to obtain the voltage offset $\Delta E_1(U_{jet})$ and ΔE_2 (U_{jet}). **e** Comparison between voltage pairs from the *accurate* and the misaligned calibration, with the latter shifted after application of the voltage offset estimated in **d**

to various known free-stream (or centerline) speeds. This calibration is similar to the conventional calibration for a single-wire hotwire sensor (Talluru et al. 2014) and is the reference 'zero-angle' calibration used by Baidya et al. (2019a) to check for misalignment between the tunnel and the jet calibrator coordinate system. For an accurately aligned jet calibrator, the voltage pairs corresponding to $\theta = 0°$ (from the 2-D calibration) should align with the voltage pairs recorded during 1-D calibration, meaning that the jet flow direction (at $\theta = 0°$) is parallel to the streamwise direction x. Apart from this, the 1-D calibration is also used to take into account the drift of the hotwire sensors over time, with the calibration conducted both before (pre 1-D) and after (post 1-D) the velocity profile measurement. In addition to this, the X-probe was also periodically traversed to the free-stream during the measurement to acquire one additional voltage–velocity relationship, following a practise known as 'free-stream' checks proposed by Talluru et al. (2014). These checks, combined with the pre and post 1-D calibrations, are used to obtain an updated 1-D calibration (via interpolation) for each wall-normal location of the profile. In the case of an X-probe, however, the u and v (or w) information is retrieved from the 2-D calibration surfaces, $f(E_1, E_2)$ and $g(E_1, E_2)$, respectively. We utilize the interpolated 1-D calibrations as references to subsequently generate new 2-D calibration surfaces for each wall-normal location to account for the sensor drift. This procedure is discussed in detail in "Appendix 1" (Sect. 8).

In the case of measurements in HRNBLWT, the jet calibrator could be setup inside the test section. This allowed for an accurate alignment of the jet coordinate system with the tunnel coordinate system through the use of laser sheets. This involved creating laser sheet planes parallel and perpendicular to the tunnel side walls which were used as references for the alignment procedure, ensuring $\phi', \psi' \approx 0°$ (Fig. 1). This position of the jet was set as the reference position ($\theta = 0°$) for the jet encoders. Hence, an '*accurate*' 2-D calibration (i.e., one without any misalignment) of the X-probe could be achieved during the boundary layer measurement. Another calibration was carried out for the same X-probe, immediately after the *accurate* 2-D calibration, where the jet was intentionally aligned via visual inspection only (i.e., without using the laser sheets), resulting in $\phi', \psi' \neq 0°$ (refer Sect. 3).

During channel flow measurements, given the limited cross section of the working section (1170×100 mm^2), the jet facility was positioned on the top outer surface of this section. The X-probe was hence traversed outside of this section, using the linear rail mechanism, for conducting the 2-D calibration. However, unlike the case of HRNBLWT, there were no reliable reference planes at the channel top for accurately aligning the jet using laser sheets. Irrespectively, due to physical restrictions, it was not possible to setup a laser arrangement on the channel top surface. Hence, the alignment of the jet was always carried out through visual inspection, a method which is prone to misalignment ($\phi', \psi' \neq 0°$). Accordingly, as marked in Table 1, all the 2-D calibrations in the case of the channel flow measurements were misaligned. This was confirmed on comparing these calibrations with the reference 1-D calibration as discussed previously. The 2-D calibration in HRNBLWT, where the jet was aligned via visual inspection only, was conducted to mimic the situation experienced during channel measurements.

2.2 Synthetic experiments

Here, since the focus is on canonical wall-bounded flows, synthetic probe experiments were conducted on published DNS fields of a turbulent channel flow at $\mathrm{Re}_\tau = 934$ (del Alamo et al. 2004). It is to be noted that the Re_τ for this dataset is very close to the physical experiments in the channel flow facility. Researchers interested in implementing the correction scheme for measurements in other flow configurations, for example APG TBL flow, would have to select a corresponding APG TBL DNS dataset. The synthetic experiments are based on the argument that the spatial attenuation corresponding to sensor measuring volume scales with viscous units (i.e., independent of Re_τ). The resolution of the original DNS data set in the streamwise-spanwise ($\Delta x^+ \times \Delta y^+$) plane is 7.6×3.8, better than any of the physical experiments in the channel (Table 1). In the present study, we compare the spatially filtered statistics from the synthetic experiments with those from physical experiments and the differences between the two are assigned to calibration misalignment. To this end, spatially filtered velocity fields are computed for each X-probe measuring volume and probe type mentioned in Table 1, from which the statistics and spectra are obtained at the same wall-normal locations as the corresponding physical experiment (limited up to $z^+ \leq 934$). All the statistics and spectra presented here are averaged over 15 similarly spatially filtered DNS flow fields to obtain a reasonable convergence. Interested readers may refer to Philip et al. (2013) or Baidya et al. (2019b) for more details on the methodology adopted for these synthetic experiments. It is important to note here that these synthetic experiments imitate the approach through which instantaneous velocity is obtained from the X-probe sensor in a physical experiment, i.e., by computation of the effective velocities over the sensor length. It is thus different from a simple box filtering approach across the measuring volume which is done while emulating PIV datasets (Lee et al. 2016).

With the focus being on wall-bounded flows in the present study, we primarily utilize the viscous-scaled premultiplied energy spectra obtained from the synthetic experiments to correct our experimental observations. A database ("Appendix 4") of this spectra, obtained for varying X-probe

geometric parameters: l^+, Δs^+ and θ^w, has been compiled and provided for convenience of the researchers who are interested in utilizing the correction scheme being proposed later in Sect. 4.2. In case of measurements in other flow configurations, however, researchers interested in implementing this correction scheme would have to choose a relevant DNS dataset and utilize the scaling behavior relevant to the flow. For example, Burattini et al. (2007) in their study of an isotropic flow, used the Batchelor scaling argument to correct their X-probe measurements using an isotropic flow DNS.

3 2-D calibration misalignment

In this section, we discuss possible ways to identify and account for calibration misalignment before generating the calibration surfaces for processing the velocity time series. For this, we consider the two 2-D calibrations - *accurate* and misaligned (refer Sect. 2.1.3), conducted for a *uv-CX* probe before the high Re_τ measurement in HRNBLWT (Table 1). Both these calibrations are used to process this boundary layer data set and compute the velocity statistics and spectra, allowing us to observe the effect of misalignment on these statistics.

3.1 2-D calibration misalignment: identification and subsequent processing

Figure 2 gives a flowchart-type description of identifying a misaligned calibration followed by two possible ways of accounting for it while processing. We begin by considering the mean voltages in Fig. 2b associated with the accurate and misaligned 2-D calibration, along with the pre 1-D calibration interpolated over the same range of U_{jet}. The difference between the misaligned and the *accurate* 2-D calibration is apparent. It can be noted that a similar voltage pair is recorded at the lowest U_{jet} ($U_{\mathrm{jet}} \approx 0$) during both the 2-D calibrations and they differ only for higher U_{jet}, suggesting that the mismatch is an artifact of misalignment and not sensor drift. The angular offset for the misaligned calibration, which is representative of the in-plane misalignment angle (ϕ'), is estimated to be $+\,2.5°$ approximately by following the procedure outlined by Baidya et al. (2019a) (Sect. 1; Fig. 2c) and can be accounted for in the calibration map as shown in the flowchart. Here, ϕ' is positive for counterclockwise orientation and negative for clockwise orientation. This method, however, doesn't account for the out-of-plane misalignment angle (ψ') since its effect does not show up as an angular offset, as seen for ϕ', in an X-probe calibration. The 'angular-offset' map is then inverted to obtain the calibration surfaces f_1' and f_2' for u and v, respectively. This method is henceforth referred as the angular offset (AO) method.

Given that the estimated ϕ' lies beyond the scope of correction of the AO method (Baidya et al. 2019a), we propose another method to account for misalignment wherein ϕ', ψ' are forced to 0° by offsetting the calibration voltages instead of the jet angles. We do this by forcing the 2-D calibration voltage pairs recorded for $\theta = 0°$ at various U_{jet} (henceforth referred as θ_o points), to be equivalent to those recorded during the 1-D calibration (Fig. 2d). Based on the comparison, unique voltage offsets $\Delta E_1(U_{\mathrm{jet}})$ and $\Delta E_2(U_{\mathrm{jet}})$ are estimated for both the sensors which are applied across the entire calibration map for the corresponding U_{jet}. Figure 2e shows the resulting 'voltage-offset' 2-D calibration which gives another pair of calibration surfaces for u (f_3') and v (f_4') on inversion. It can be noted that the 'voltage-offset' calibration map, in general, is still different compared to the *accurate* 2-D calibration map shown in the background. This is because of the estimated voltage offsets being a function of U_{jet} only, effectively assuming that the hotwire sensor responds linearly to the change in flow angle. This assumption, however, is incorrect given the known fact about the nonlinear response of the sensor to flow angles (Hinze 1975; Bradshaw 2013) the consequences of which will be discussed ahead. This method of accounting for misalignment is henceforth referred as voltage offset (VO) method. We shall compare the performance of the two methods in the forthcoming discussion.

3.2 2-D calibration misalignment: effect on velocity statistics and spectra

We now process the high Re_τ boundary layer dataset using the two different sets of calibration surfaces obtained from the misaligned 2-D calibration (i.e., AO and VO), in addition to using the calibration surfaces obtained from the *accurate* 2-D calibration. The statistics obtained on processing via the *accurate* 2-D calibration compare well with results of Baidya et al. (2012) (not shown here) at a similar Re_τ and are being used simply as a reference to bring out the effect of a misaligned 2-D calibration. Comparing and contrasting the statistics obtained from the AO method with those from the VO method in Fig. 3, the latter performs better than the former by at least yielding reasonably accurate streamwise statistics. Poor performance by the AO method was expected since $|\phi'| > 0.5°$ (Baidya et al. 2019a), and hence only the VO method of processing the misaligned calibration is considered henceforth. In Fig. 3, the terminology 'viscous-scaled streamwise turbulence intensity' refers to the variance of the streamwise velocity fluctuation normalized by the square of the friction velocity (i.e., $\overline{u^2}^+ = \overline{u^2}/U_\tau^2$). Readers should note that a similar terminology has been used to refer to the normalized variance of all the velocity components throughout this manuscript.

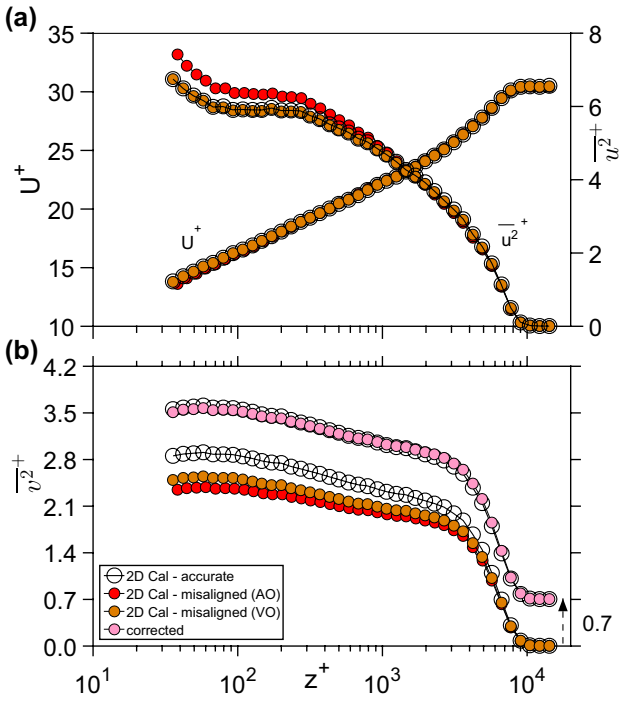

Fig. 3 Viscous-scaled profiles of **a** mean streamwise velocity and streamwise turbulence intensity and **b** spanwise turbulence intensity obtained on processing the high Re_τ boundary layer data set using the *accurate* and misaligned 2-D calibrations. In case of the misaligned calibration, data processing is carried out using both AO and VO methods. In **b**, the corrected turbulence intensity is plotted with a vertical shift and compared with $\overline{v^2}^+$ obtained from the *accurate* 2-D calibration

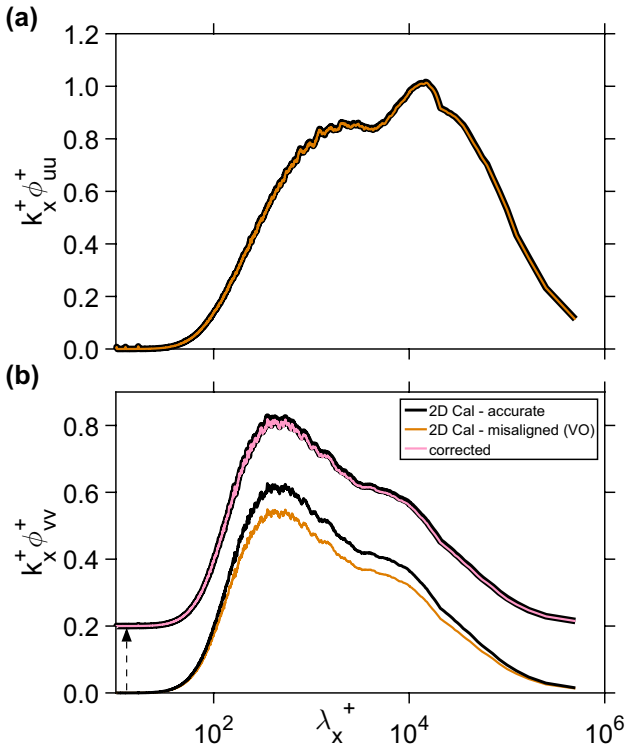

Fig. 4 Viscous-scaled 1-D premultiplied streamwise energy spectra of the **a** streamwise and **b** spanwise velocity obtained on processing the high Re_τ boundary layer data set using the *accurate* and misaligned 2-D calibrations. In case of the misaligned calibration, data processing is carried out using the VO method only. In **b**, the corrected spectra of the spanwise velocity is plotted with a vertical shift and compared with spectra obtained from the *accurate* 2-D calibration

The fact that $\overline{v^2}^+$ estimated from the VO method deviates from the reference values may be attributed to the application of a voltage offset ($\Delta E_1(U_{\text{jet}})$, $\Delta E_2(U_{\text{jet}})$) independent of θ, incorrectly assuming a linear response of the hotwire sensor to flow angles. To further investigate this, we compare the viscous-scaled premultiplied 1-D streamwise energy spectra of both the streamwise ($k_x^+\phi_{uu}^+$) as well as spanwise ($k_x^+\phi_{vv}^+$) velocity components at $z^+ = 100$ in Fig. 4. Although $k_x^+\phi_{uu}^+$ processed via misaligned calibration compares well with the reference spectra, $k_x^+\phi_{vv}^+$ from the misaligned calibration seems to be attenuated across the entire range of scales (λ_x^+). However, the shape/form of the erroneous spectra is similar to that of the reference spectra and a similar observation is noted at all z^+. Here, $\lambda_x = 2\pi/k_x$ where k_x is the streamwise wave number and is obtained from the temporal frequency by invoking the Taylor's hypothesis which assumes the convection velocity (U_c) for all scales to be equal to $U(z^+)$. Since $\overline{v^2}^+(z^+) = \int_0^\infty k_x^+\phi_{vv}^+(\lambda_x^+;z^+)\,\mathrm{d}(\ln\lambda_x^+)$, the comparison between the spectra can explain why the $\overline{v^2}^+$ profile from the misaligned calibration appears to be an attenuated version of the reference profile (Fig. 3b). Based on this observation, we hypothesize that a misaligned calibration, when processed via the VO method, yields lateral velocity variance which is an amplified/attenuated version of the accurate one. The method, however, estimates the relative energy distribution across the entire range of scales in the flow reasonably accurately. The nature of deviation, i.e., amplification or attenuation, is dependent on the voltage offset ($\Delta E_1(U_{\text{jet}})$ and $\Delta E_2(U_{\text{jet}})$) applicable for the respective case, as is shown ahead.

The aforementioned hypothesis can be confirmed by systematically varying ϕ' (Fig. 2) and investigating its effect on the processed statistics, $\overline{u^2}^+$ and $\overline{v^2}^+$. The availability of the functions $E_1 = f_1(U_{\text{jet}}, \theta)$ and $E_2 = f_2(U_{\text{jet}}, \theta)$, obtained via the EAM (refer Sect. 2.1.3) for the 'accurate' 2-D calibration, facilitates such an investigation wherein

known misalignments, atleast in the sensor plane, can be introduced artificially during the data reduction process. To this end, the functions are used to generate new 2-D calibration maps such that ϕ' systematically varies between $-5° \le \phi' \le 5°$. These maps are then 'voltage-offset' by following the same procedure as outlined in Fig. 2 and then used to process the high Re_τ boundary layer dataset. Figure 5a, b, respectively, shows the $\overline{u^2}^+$ and $\overline{v^2}^+$ processed from these calibration maps with known angular misalignments. Consistent with what is observed in Fig. 3, $\overline{u^2}^+$ is estimated reasonably accurately via the VO method for the ϕ' range considered. While, $\overline{v^2}^+$ appears to be: (1) amplified when $\phi' < 0$ and (2) attenuated when $\phi' > 0$, as compared to $\overline{v^2}^+$ estimated via the 'accurate' 2-D calibration ($\phi' = 0°$). Not surprisingly, the degree of attenuation/amplification increases with increase in the severity of misalignment (i.e., $|\phi'|$). With the hypothesis confirmed, we now utilize this property to propose a scheme to correct the erroneous spanwise spectra in Fig. 4b by estimation of a correction ratio which can be used as a *gain* to amplify the spectra.

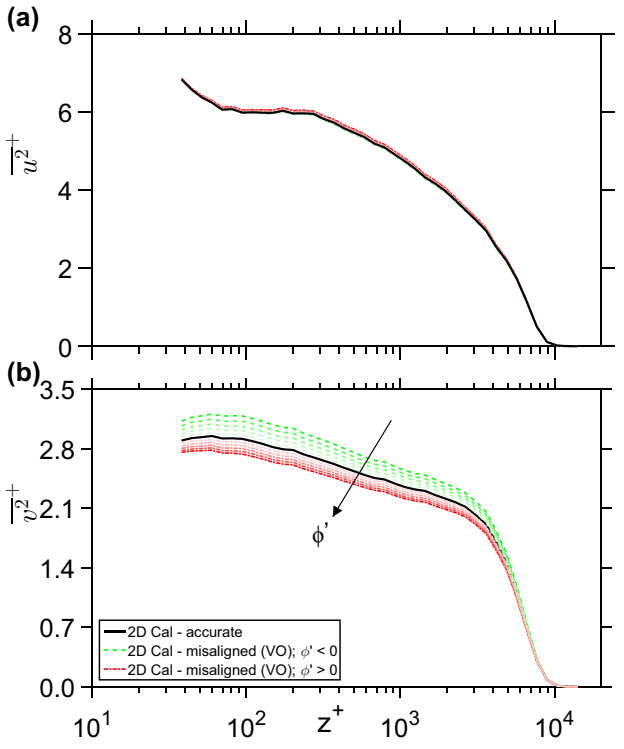

Fig. 5 Viscous-scaled profiles of **a** streamwise and **b** spanwise turbulence intensity obtained on processing the high Re_τ boundary layer data set using 2-D calibrations with known misalignments in the range $-5° < \phi' < 5°$. Dashed green lines represent $\phi' < 0$, while dot-dashed red represent $\phi' > 0$ with the shading intensity increasing with the degree of misalignment for both cases. Note that all calibrations are processed via the VO method only

4 Correction scheme

4.1 Re_τ invariance of the turbulent kinetic energy in the small scales

The correction scheme is based on the premise that the viscous-scaled small-scale turbulence energy is invariant with Re_τ and solely depends on the viscous-scaled spatial resolution of the sensor measuring the velocity fluctuations. Hutchins et al. (2009) have demonstrated this previously for $\overline{u^2}^+$, while Baidya et al. (2012) and Baidya (2016) have demonstrated the same for $\overline{v^2}^+$ and $\overline{w^2}^+$. Here, we analyze various turbulence datasets, with Re_τ spanning $O(10^3)$–$O(10^4)$, to establish a spectral cutoff (λ_x^+) for which the premise would be true for all three velocity components. Further on, we highlight how the data processed from misaligned 2-D calibrations is inconsistent with the premise.

Datasets considered are the channel DNS at $Re_\tau \approx 1000$ and 5200 (Lee and Moser 2015), ZPG TBL DNS at $Re_\tau \approx 2000$ (Sillero et al. 2013) and the present experimental dataset for the ZPG TBL at $Re_\tau \approx 10{,}000$ (Table 1) processed using an *accurate* 2-D calibration. Also considered are the statistics from the synthetic experiment, with X-probe volume corresponding to the high Re_τ experimental dataset, to take into account the attenuated small-scale energy due to the spatial resolution issue. It was found, based on careful observation, that energy contained in the scales smaller than $\lambda_x^+ \approx 210$ is consistent with the premise. To prove this, Fig. 6 showcases the turbulence stress profiles from the aforementioned datasets, decomposed into small-scale ($\overline{u_{i,S}^2}^+$) components considering $\lambda_x^+ \approx 210$ as the cutoff. Here, since $\overline{u_i^2}^+(z^+) = \int_0^\infty k_x^+ \phi_{ii}^+(\lambda_x^+; z^+)\, \mathrm{d}(\ln \lambda_x^+)$, hence $\overline{u_{i,S}^2}^+(z^+) = \int_0^{210} k_x^+ \phi_{ii}^+(\lambda_x^+; z^+)\, \mathrm{d}(\ln \lambda_x^+)$ for $i = u$, v or w. The cutoff considered here is much smaller than that considered in the literature (Hutchins et al. 2009; Baidya et al. 2012) due to the minimum Re_τ among selected data sets being as low as 934. The good comparison among various datasets, with comparable spatial resolutions, gives a convincing evidence supporting the premise. Also, the small-scale energy component for a boundary layer (external) flow matches well with that for channel (internal) flow (Monty et al. 2009), making the premise valid for all canonical wall-bounded flows. It should however be noted that the overlap between $\overline{u_{i,S}^2}^+$ from the physical and synthetic experiments is best closest to the wall and the two profiles deviate gradually as we go away from the wall ($z^+ > 300$). This has also been noted by Hutchins et al. (2009) and Lee et al. (2016) for high Re_τ experimental datasets, at $z/\delta > 0.5$, and is likely an artifact of the decreasing small-scale energy content in the outer region of the flow.

With $\lambda_x^+ \approx 210$ established as a reasonable spectral cutoff, one should ideally see an overlap of $k_x^+ \phi_{ii}^+(\lambda_x^+; z^+)$ at

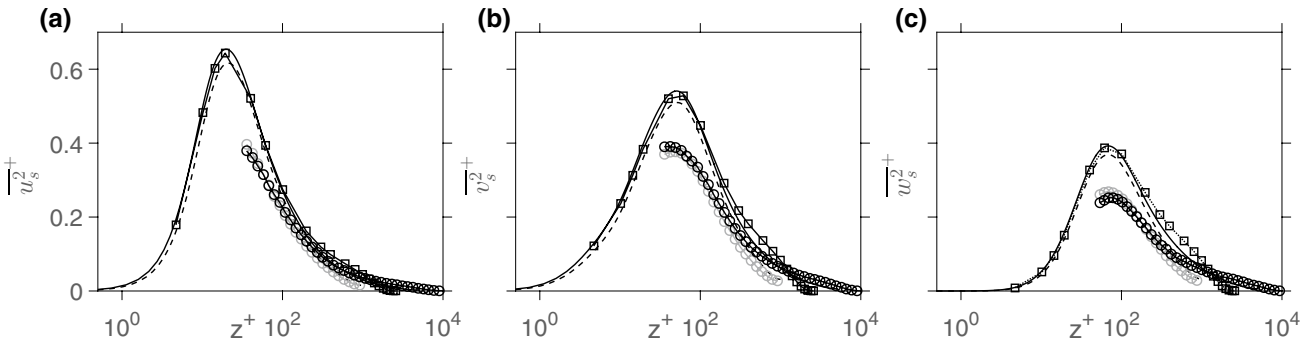

Fig. 6 Viscous-scaled turbulence intensity profiles of the **a** streamwise, **b** spanwise and **c** wall-normal velocity decomposed into small-scale component based on a cutoff wavelength of $\lambda_x^+ \approx 210$ for various data sets: lines (**- -**) and (**-**) represent channel DNS data at $\mathrm{Re}_\tau = 1000$ and 5200, respectively (Lee and Moser 2015). (□) Represents ZPG TBL DNS data at $\mathrm{Re}_\tau \approx 2000$ (Sillero et al. 2013). (○) In dark shading represent ZPG TBL data from present physical experiments at $\mathrm{Re}_\tau \approx 10{,}000$ processed via *accurate* 2-D calibration, while those in light shading represent statistics from the corresponding synthetic experiments

various Re_τ at least for $\lambda_x^+ < 210$, where $i = u$, v or w. Ganapathisubramani (2018) has previously demonstrated this to be true for the experimentally acquired $k_x^+\phi_{uu}^+$. With the intention to establish the basis for the correction scheme, we consider $k_x^+\phi_{ii}^+$ at $z^+ \approx 100$ (Fig. 7) from datasets at $\mathrm{Re}_\tau \approx 1000$ and 10,000 processed using the misaligned 2-D calibration for CX probe. Also plotted is the premultiplied spectra obtained from the corresponding synthetic experiments, which form a part of the database being shared for convenience of interested users. As expected from Fig. 4a, the experimentally obtained premultiplied spectra of u ($(k_x^+\phi_{uu}^+)_{\mathrm{Exp}}$) matches reasonably well with its counterpart from the synthetic experiment ($(k_x^+\phi_{uu}^+)_{\mathrm{sDNS}}$) for $\lambda_x^+ < 210$. On the other hand, $(k_x^+\phi_{vv}^+)_{\mathrm{Exp}}$ and $(k_x^+\phi_{ww}^+)_{\mathrm{Exp}}$) appear to be either amplified or attenuated compared to their counterparts from the synthetic experiments in the same scale range. Drawing inspiration from our earlier discussions based on Fig. 4b, the mismatch we observe in Fig. 7b, c is also considered to be an artifact of using a misaligned calibration. Based on the aforementioned premise, we propose a methodology to force a collapse of $(k_x^+\phi_{vv}^+)_{\mathrm{Exp}}$ and $(k_x^+\phi_{ww}^+)_{\mathrm{Exp}}$ onto the corresponding $(k_x^+\phi_{vv}^+)_{\mathrm{sDNS}}$ and $(k_x^+\phi_{ww}^+)_{\mathrm{sDNS}}$ for $\lambda_x^+ < 210$, by computing a correction ratio.

4.2 Defining the correction scheme

We propose to compute a ratio (r) for every z^+ as follows:

$$r(z^+) = \overline{\left(\frac{(k_x^+\phi_{ii}^+(\lambda_x^+;z^+))_{\mathrm{sDNS}}}{(k_x^+\phi_{ii}^+(\lambda_x^+;z^+))_{\mathrm{Exp}}} \right)} \tag{1}$$

for $i = v$ or w and $190 < \lambda_x^+ < 210$, with the overbar indicating averaging over this range. The ratio r is computed individually at each z^+ up to $z^+ = 934$, which is limited by the DNS dataset. We consider the mean value, $r^c = \overline{r(z^+)}$ for $0 < z^+ < 300$ as the unique correction ratio for the entire velocity profile. Figure 8 depicts the percentage deviation of $r(z^+)$ from r^c, across all wall-normal spacings, for all the velocity profile measurements listed in Table 1. r^c appears to be a reasonably good representative value since r doesn't vary significantly with z^+, at least for low Re_τ channel measurements.

Next, the correction ratio r^c is used as a *gain* to amplify or attenuate the premultiplied 1-D spectra as follows: $(k_x^+\phi_{ii}^+)^c_{\mathrm{Exp}} = r^c(k_x^+\phi_{ii}^+)_{\mathrm{Exp}}$ for $i = v$ or w, where $(k_x^+\phi_{ii}^+)^c_{\mathrm{Exp}}$ is the corrected spectra. Figure 9 shows the corrected version of the premultiplied 1-D spectra shown in Fig. 7. It can be observed that although r^c was estimated purely based on the spectra in the range $190 < \lambda_i^+ < 210$, the corrected spectra shows a reasonable overlap with the corresponding $(k_x^+\phi_{ii}^+)_{\mathrm{sDNS}}$ in the entire small-scale range, $\lambda_x^+ < 210$, and for both the low (channel) and high Re_τ (boundary layer) cases. This is observed for the spectra at all z^+. It suggests that a unique correction ratio (r^c) for the entire velocity profile performs reasonably well. The comparison between $(k_x^+\phi_{ii}^+)^c_{\mathrm{Exp}}$ from the channel flow experiment with the corresponding $(k_x^+\phi_{ii}^+)_{\mathrm{sDNS}}$ is especially interesting due to the Re_τ for the two cases being similar. After correction, the spectra seem to match reasonably well for the entire range of scales, λ_x^+.

It is to be noted that for estimating r^c, $z^+ \approx 300$ was considered as an upper bound because of a gradual deviation of $r(z^+)$ from r^c for $z^+ > 300$, seen consistently for all cases, especially for the high Re_τ measurements. It should be noted that a mismatch was observed between the $\overline{u_{i,S}^2}^+$ profiles (Fig. 6b, c), in the similar wall-normal range, likely due to the decreasing small-scale energy content in the outer region of the flow. Further, in Eq. 1, only a subset of the

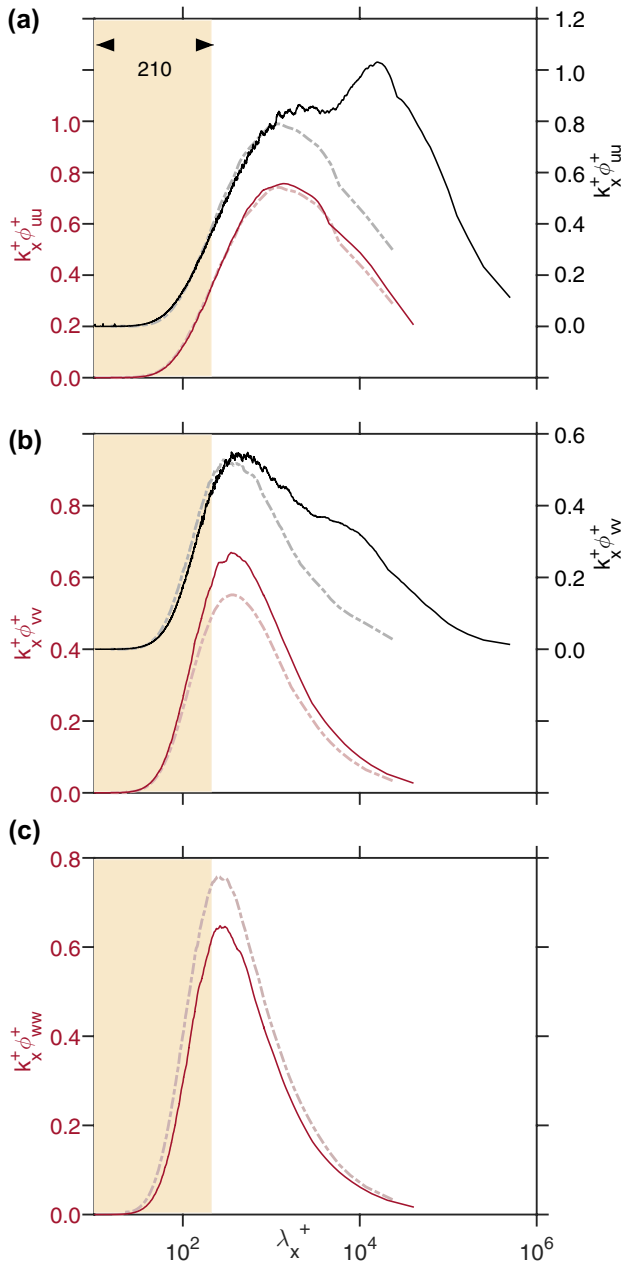

Fig. 7 Viscous-scaled premultiplied energy spectra of the **a** streamwise, **b** spanwise and **c** wall-normal velocity components at $z^+ \approx 100$ for $Re_\tau \approx 10{,}000$ ZPG TBL data set (heavy black) and $Re_\tau \approx 1000$ channel data set (dark red) acquired using *CX* probe (Table 1) and processed using a misaligned 2-D calibration. Dot-dashed lines in light shading represent data from the synthetic experiments corresponding to the probe volume in the physical experiments. The yellow background highlights the wavelength range $0 < \lambda_x^+ < 210$

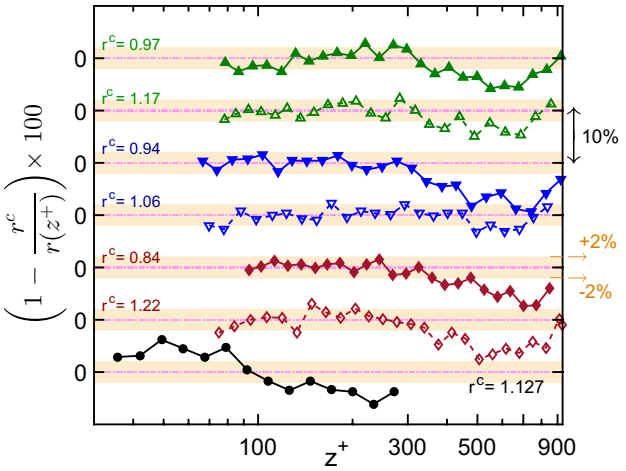

Fig. 8 Percent deviation of r from the correction ratio r^c across the measurement locations (z^+), computed for the physical experiments with a misaligned calibration. Symbols represent physical experiments with various X-probes as mentioned in Table 1, with (–) and (- -) line types representing a *uv* and *uw* X-probe, respectively. For the case of high Re_τ experimental data (○), deviations only up to $z^+ \approx 300$ have been shown. Zero labels corresponding to each profile are vertically offset by 10% from one another and the light yellow background highlights deviation in the range ± 2% for each profile

small-scale range $\lambda_i^+ < \lambda_x^+ < 210$, with $\lambda_i^+ = 190$ instead of 0, has been considered for the purpose of computing the ratio, $r(z^+)$. This is because the magnitude of $k_x^+\phi_{ii}^+$ ($i = v$ or w) for the smallest scales drops significantly with increase in z^+ (Baidya et al. 2012, 2017). In addition, inaccuracies due to experimental uncertainty or noise also influence the spectra in the smallest scales, thereby leading to non-physical values of the ratio $r(z^+)$. A sensitivity analysis was carried out (not shown here) to quantify the effect of varying λ_i^+ on the value of $r(z^+)$. It was found that the ratio changes within ± 2% for $130 < \lambda_i^+ < 190$. For $\lambda_i^+ < 130$, the change is significant.

With the correction scheme established, we shift our focus to correcting the time series of the lateral velocity fluctuations by using r^c. Essentially, the corrected time series can be obtained by simply performing an inverse Fourier transform on the corrected energy spectra, $(k_x^+\phi_{ii}^+)_{\text{Exp}}^c$ for $i = v$ or w. The complete methodology to obtain the corrected v (or w) time series has been presented in "Appendix 2," with Eq. 3 giving the final result. In the next section, we compare the uncorrected and corrected statistics, computed from the respective velocity time series, for all the measurements shown in Table 1.

5 Comparing uncorrected and corrected statistics

Figure 10 depicts the uncorrected and corrected statistics from the channel flow measurements using various X-probes. Also plotted in parallel are the statistics from the corresponding synthetic experiments as well as from

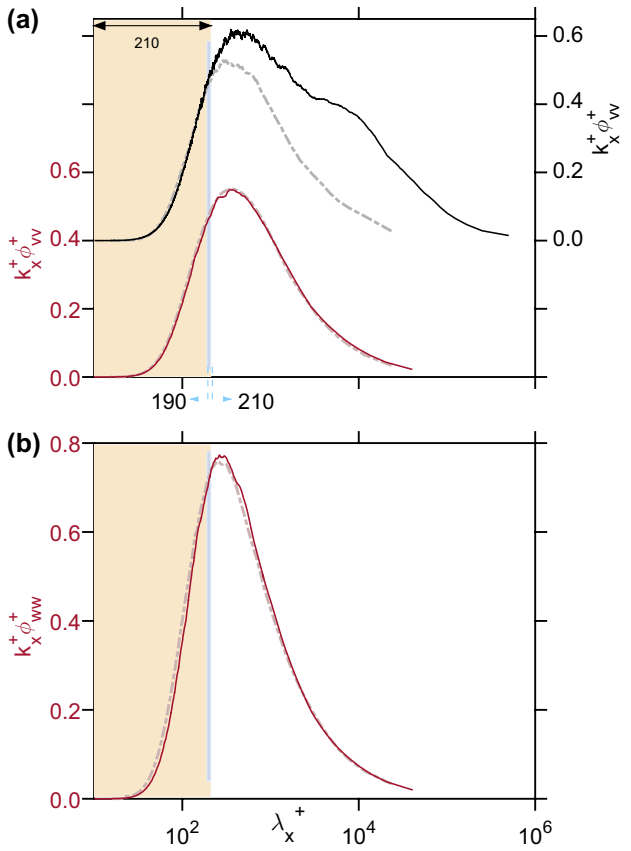

Fig. 9 Corrected viscous-scaled premultiplied energy spectra of the **a** spanwise and **b** wall-normal velocity components at $z^+ \approx 100$ for $Re_\tau \approx 10,000$ ZPG TBL data set (heavy black) and $Re_\tau \approx 1000$ channel data set (dark red) acquired using *CX* probe (Table 1) and processed using a misaligned 2-D calibration. Dot-dashed lines in light shading represent spectra from the synthetic experiments corresponding to the probe volume in the physical experiments. The yellow and blue backgrounds highlight the wavelength range $0 < \lambda_x^+ < 210$ and $190 < \lambda_x^+ < 210$, respectively

the well-resolved (unfiltered) fields of the channel DNS data set. It should be noted that only those statistics which are associated with the lateral velocity fluctuations ($\overline{v^2}^+$, $\overline{w^2}^+$ and $\overline{uw}^+$) required a correction since $\overline{u^2}^+$ is estimated reasonably accurately after implementation of the VO method (refer Sect. 3.2). It is evident that the uncorrected statistics (Fig. 10; left column), which differ from the synthetic experiment estimates by up to 10%, compare reasonably well after correction (Fig. 10; right column) for all X-probes. On correction, the statistics differ by at the most 4% for $-\overline{uw}^+$, and upto 2% for the normal stresses, which is within acceptable experimental uncertainty (Baidya et al. 2019a). Here, the percentage difference has been calculated at $z/h \approx 0.1$ ($z^+ \sim 100$) for the *AX*1 X-probe following:

$$\text{Percent error} = \left| \frac{(\overline{u_i u_i}^+)_{\text{Exp}} - (\overline{u_i u_i}^+)_{\text{sDNS}}}{(\overline{u_i u_i}^+)_{\text{sDNS}}} \right| \times 100, \tag{2}$$

where i is used to denote velocity fluctuations along x, y or z.

The correction technique is also applied to the high Re_τ measurements in the boundary layer and its effectiveness is shown in Figs. 3b and 4b plotted earlier. $\overline{v^2}^+(z^+)$ and $(k_x^+\phi_{vv}^+)(\lambda_x^+, z^+ \approx 100)$, processed using misaligned 2-D calibration, is corrected and compared with the statistics processed using the *accurate* 2-D calibration. A reasonably good match is observed on comparison, reinforcing the effectiveness of the correction technique across a decade of Re_τ variation. It would also be worthwhile to comment on the second part of the premise, forming the basis for the correction scheme, which argues that the viscous-scaled energy in the small-scales is a function of the X-probe spatial resolution. It is for this reason that filtered DNS estimates corresponding to each X-probe measuring volume (Table 1) need to be considered for successful implementation of the scheme. Interested readers may refer to "Appendix 3" where the velocity statistics from (1) the corrected experimental time series and (2) the synthetic experiment have been shown to be following consistent trends for varying spatial resolution of the X-probes, reaffirming the effectiveness of the scheme.

6 Summary of the steps for implementing the correction scheme

With the correction scheme established, here we summarize the steps to be followed while implementing the scheme for any turbulent shear flow measurement, in general. References are provided, wherever required, to the relevant section in the manuscript where the specific procedure has been discussed in detail.

1. Choose an appropriate X-probe configuration for the flow being investigated (Sect. 2.1.2).
2. After the measurements are conducted, check the 2-D calibration for misalignment by comparing the voltage pairs corresponding to the θ_o points with the 1-D calibration (Fig. 2d).
3. If an angular offset is observed on comparison, implement the VO method to obtain the 'voltage-offset' calibration map (Sect. 3.1).
4. Process the data by using the new calibration map. It is this dataset which will be corrected with the help of a DNS database as a reference, based on a scaling behavior characteristic of the flow.
5. Select the appropriate DNS dataset (Sect. 2.2) for the flow being measured and obtain the filtered estimates corresponding to the X-probe volume.

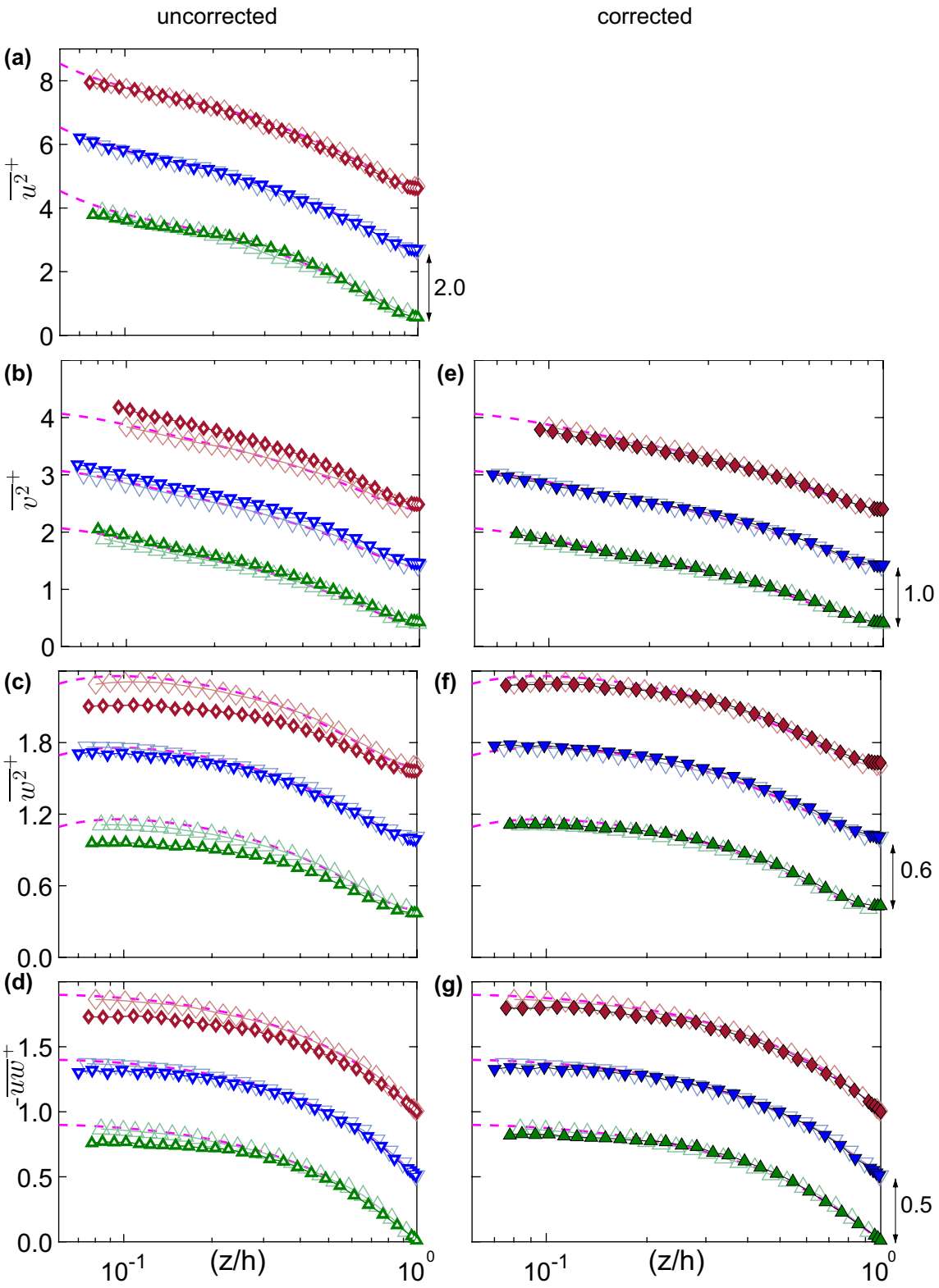

Fig. 10 The uncorrected (dark, partially-filled) and corrected (dark, fully-filled) **a** streamwise, **b**, **e** spanwise, **c**, **f** wall-normal and **d**, **g** Reynolds shear stresses for the $\mathrm{Re}_\tau \approx 1000$ channel flow experiments. The uncorrected statistics are plotted in **a**–**d**, while the corrected ones are plotted in **e**–**g**. Symbols represent experiments with various X-probes as mentioned in Table 1. Empty symbols in light shading represent statistics from the corresponding synthetic experiments. Dashed line in magenta represents the unfiltered statistics from the channel DNS at $\mathrm{Re}_\tau = 934$. Note the vertical shift in profiles

6. Choose the relevant scaling, depending on the flow type, for comparing the experimental and filtered DNS results (Sect. 2.2).
7. Check if the *u*-statistics obtained from the measurements overlap with the filtered DNS estimates in the relevant scale range (Sect. 3.2).
8. To correct the *v*/*w* statistics, use Eq. 1 and the associated methodology given in Sect. 4.2 to determine the unique correction ratio (r^c) for the measurements.
9. On determination of r^c, correct the entire time series of *v*/*w* by following the methodology given in "Appendix 2." Recompute the statistics from the corrected time series and compare with the filtered DNS to verify the correction.

7 Summary and conclusions

The present study experimentally investigated the effect of misalignment between the calibration and tunnel coordinate system for an X-probe calibration. The emphasis was on scenarios where the calibration is severely misaligned ($|\phi'| > 2°$) due to the absence of reference planes required to accurately orient the calibration jet with the probe. Since the previously used methodology of offsetting the calibration jet angles by ϕ' (Baidya et al. 2019a; Zimmerman et al. 2017) fails to provide acceptable velocity statistics, a new methodology based on offsetting the calibration voltages was implemented to account for the misalignment. It was found that the streamwise velocity statistics processed from such a calibration agreed reasonably well with the reference statistics from the *accurate* (well-aligned) calibration. Normal stresses of the lateral velocity components, however, appeared to be either amplified or attenuated relative to the reference profiles. Analysis of the corresponding energy spectra revealed that the energy is amplified/attenuated across the entire range of scales by a *gain*. Subsequently, it was hypothesized that a misaligned calibration does not influence the relative energy distribution in the energy spectra but simply magnifies/dampens it by a factor. A separate analysis ("Appendix 1"), conducted with a calibration map obtained from a *drifted* X-probe sensor, confirmed that these observations were not an artifact of the drift in the sensor voltages with time.

The consistent nature of deviation of the erroneous statistics, from the reference statistics, inspired the proposal of a correction scheme to rectify such errors arising in any other canonical wall-bounded flow experiment. The scheme is based on the premise that the viscous-scaled small-scale contributions to the turbulence stresses is invariant with Re_τ and solely dependent on the viscous-scaled spatial resolution of the probe. The spectral energy distribution obtained from the misaligned calibration is compared against the expected spectral energy distribution in the small-scale range, obtained via synthetic experiments on well-resolved DNS fields. Any differences, on comparison, were assumed to be due to calibration misalignment. Subsequently, a forced overlap of the erroneous and expected spectra was carried out in the small-scale range at each wall-normal location of the velocity profile (up to $z^+ = 934$). It yielded the ratio r which varied insignificantly in the inner-region, $z^+ < 300$. The mean, $r^c = \overline{r(z^+)}$ in this range was hence considered to be a good representative value as a unique correction ratio for the entire velocity profile. r^c was hence used to rectify the time series of the lateral velocity fluctuations, acquired across the shear flow, via Fourier analysis. Velocity statistics obtained from the corrected time series agree reasonably well with the reference statistics, for experiments conducted across a decade of Re_τ and using X-probes of varying spatial resolution. The effectiveness of the correction scheme also gives credence to the hypothesis proposed on the effect of a misaligned calibration on the processed velocity statistics, via the VO method. For the convenience of researchers interested in using this correction scheme, a database ("Appendix 4") of the premultiplied energy spectra, obtained via synthetic experiments on the channel flow for various X-probe measuring volumes, has been made openly accessible on the group website.

Acknowledgements The authors would like to thank Dr. Rio Baidya for helpful discussions and sharing his code for the synthetic experiments on the DNS data set. They also thank the authors of del Alamo et al. (2004) for making their DNS data available. Financial support of this research from the Australian Research Council (Grant No. DP180100447) is gratefully acknowledged.

Appendix 1: Accounting for the drift in hotwire voltage

It is a very well known fact that hotwire sensors drift owing to various reasons (Talluru et al. 2014) and this phenomena can lead to erroneous velocity statistics unless accounted for. In this regard, we have implemented the practice of doing periodical 'free-stream' checks (Talluru et al. 2014) for the X-probe to obtain an updated 1-D calibration curve (for both sensors) at each wall-normal location of the profile (refer Sect. 2.1.3). These 1-D calibration curves are used as references to generate unique *u* and *v* (or *w*) calibration surfaces at corresponding z^+. To this end, we process the 2-D calibrations via the voltage offset (VO) method demonstrated previously (Sect. 3.1) and show that the sensor drift is implicitly accounted on using this method. Through this, we intend to strengthen our argument that the attenuated lateral velocity statistics (shown in Figs. 3b, 4b), obtained on processing the data via the misaligned calibration, are an artifact of the misalignment and not the hotwire sensor drift.

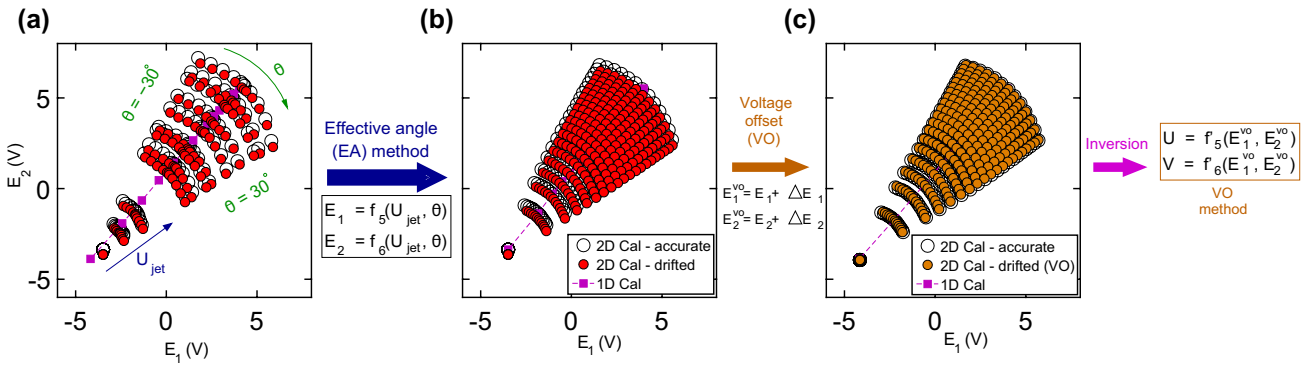

Fig. 11 Procedure to account for drift while processing 2-D calibration of an X-probe, explained by using an *accurate* 2-D calibration as a reference: **a** voltage pairs obtained by varying the U_{jet} and θ for an *accurate* and *drifted* 2-D calibration along with voltages obtained from the 1-D calibration in HRNBLWT just before the measurement. **b** Voltages in **a** interpolated onto a linearly distributed set of U_{jet} and θ based on EAM. **c** Comparison between voltage pairs from the *accurate* and *drifted* calibration, with the latter shifted after application of the voltage offset estimated by following the procedure shown in Fig. 2d

To demonstrate this, an additional *drifted* 2-D calibration, apart from the 'accurate' and misaligned 2-D calibrations, was performed on the same *uv*-CX probe used in the $Re_\tau \approx 10{,}000$ experiments in the ZPG TBL (Table 1). It was performed approximately 12 h after the end of measurement to ensure that the sensor drifts sufficiently. During this calibration, the jet coordinate system was aligned with the measurement coordinate system in the same manner as done for the *accurate* 2-D calibration, to rule out any misalignment. Figure 11a shows the raw voltage pairs acquired during the *accurate* and the *drifted* 2-D calibration on the *uv* X-probe. Also plotted are the mean voltages acquired during the 1-D calibration done immediately before the measurements. Similar to Figs. 2b and 11b shows the raw calibration voltages fitted to smooth functions of jet velocity and angles based on the EAM and solved for a linearly distributed set of U_{jet} and θ for a meaningful comparison. The difference between the *drifted* and the *accurate* 2-D calibration is pretty clear. The voltage drift is apparent from the difference between the voltage pairs from the two calibrations at $U_{jet} \approx 0$. It is different from the case of a misaligned 2-D calibration (Fig. 2b), where a difference was noted only for voltages acquired at $U_{jet} > 0$.

Following the VO method, the voltages corresponding to θ_o for the *drifted* 2-D calibration are forced to be equivalent to the 1-D calibration voltages, through which a set of unique voltage offsets ($\Delta E_1(U_{jet})$, $\Delta E_2(U_{jet})$) is estimated for both the sensors. This offset is applied across the entire calibration map, resulting in a 'voltage offset' 2-D calibration map shown in Fig. 11c. On performing the voltage shift, the difference between the *accurate* and *drifted* 2-D calibration appears to be negligible, suggesting that the effect of drift has been accounted by processing through the VO method. To confirm this, we process the boundary layer dataset acquired with the same probe via the two calibration surfaces. A good agreement is observed between the mean statistics (Fig. 12) processed via the two calibrations.

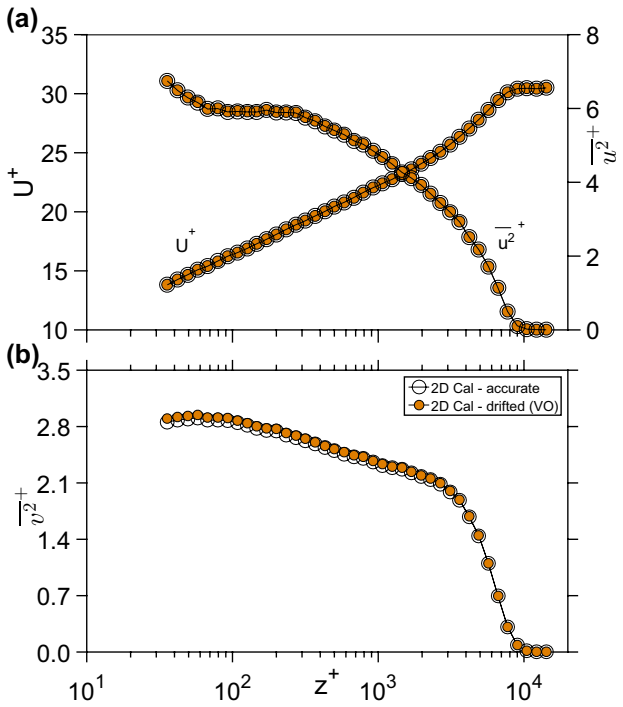

Fig. 12 Viscous-scaled profiles of **a** mean streamwise velocity and streamwise turbulence intensity and **b** spanwise turbulence intensity obtained on processing the high Re_τ boundary layer data set using the *accurate* and *drifted* 2-D calibrations. Data processing, in case of the *drifted* calibration, is carried out using the VO method

Appendix 2: Methodology to correct the time series of v or w

Let us consider the time series of the uncorrected lateral velocity fluctuations as $q(m)$, where q represents v or w and $m = 1, 2 \ldots N$ represents the discrete samples of the fluctuations with N equaling the total number of samples (sampling frequency times the total time period of acquisition). Similarly, let the corrected time series be denoted as $q^c(m)$. If $\widetilde{Q}(n)$ and $\widetilde{Q}^c(n)$ denote the complex Fourier coefficients obtained on computing the Fourier transform ($\mathcal{F}$) of $q(m)$ and $q^c(m)$, respectively, then $\widetilde{Q^c}(n) = \sqrt{r^c}\widetilde{Q}(n)$ according to the correction scheme proposed in Sect. 4.2, with n being the mode number. Here, $\sqrt{r^c}$ being real-valued will only influence the magnitude of the Fourier coefficient. The time series of the corrected velocity fluctuations can thus be found by simply computing the inverse discrete Fourier transform for $\widetilde{Q^c}(n)$:

$$q^c(m) = \mathcal{F}^{-1}[\widetilde{Q^c}(n)] = \frac{1}{N}\sum_{n=0}^{N-1} \widetilde{Q}^c(n)\exp\left(\frac{i2\pi mn}{N}\right), \text{ or}$$
$$q^c(m) = \frac{1}{N}\sum_{n=0}^{N-1} \sqrt{r^c}\widetilde{Q}_n\exp\left(\frac{i2\pi mn}{N}\right) \quad (3)$$

Appendix 3: Investigating the effect of X-probe spatial resolution

The three types of X-probes chosen to conduct experiments in the channel flow have systematically varying l^+ and Δs^+ (refer Table 1). Here, we compare the trends observed in the corrected experimental dataset, due to variation of these parameters, with those from the corresponding synthetic experiments. For brevity, we restrict ourselves solely to studying these for the *uw* X-probe.

Figure 13 shows the corrected $\overline{w^2}^+$ and $k_x^+\phi_{ww}^+$ at $z^+ \approx 100$ from the three different *uw* X-probes. The Δs^+ and l^+ trends observed in the $\overline{w^2}^+$ profiles from the corrected experimental data are consistent with those from the synthetic experiments. It is interesting to see the qualitative agreement between the pair of spectra, from the two sources, in Fig. 13b, d. For the large scales ($\lambda_x^+ > 300$), the difference in the energy distribution for varying Δs^+ is very similar in both the datasets. Similarly, for the case of varying l^+, the spectra from the corrected experimental dataset nearly overlap in the large-scale range as seen for the synthetic experiment dataset. The consistency of the corrected dataset with the synthetic experiments demonstrates the effectiveness of the correction scheme, which is facilitated by the availability

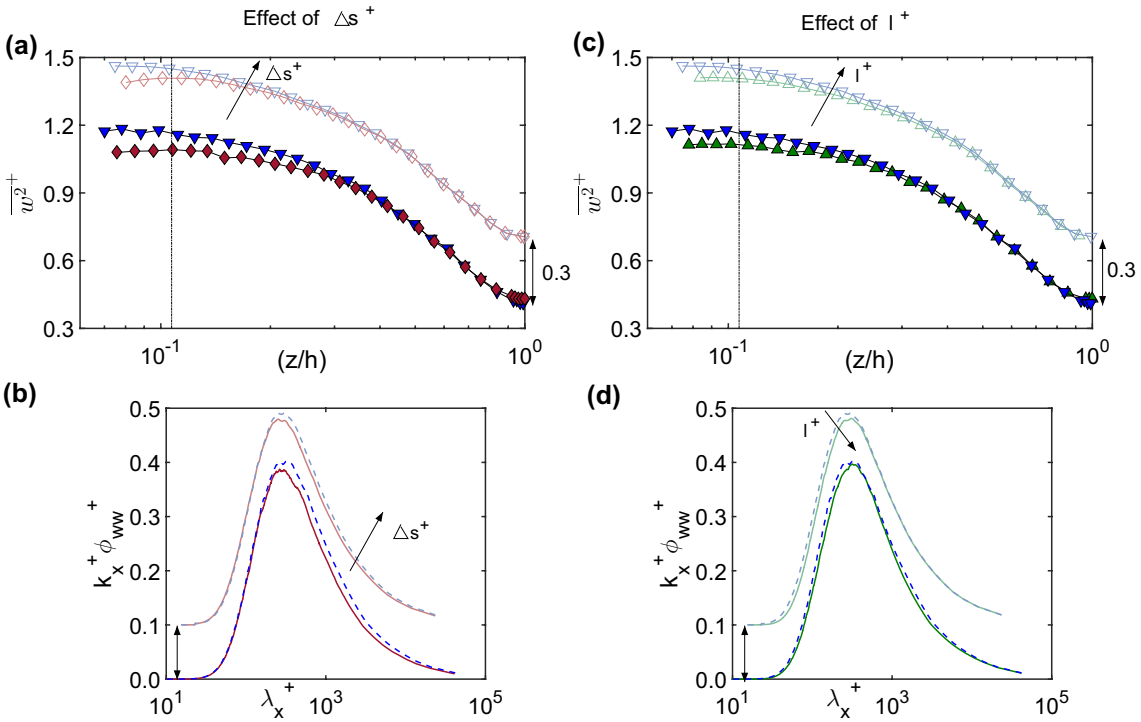

Fig. 13 **a**, **c** Corrected viscous-scaled wall-normal turbulence intensity profiles and **b**, **d** premultiplied energy spectra of the wall-normal velocity at $z^+ \approx 100$ (marked by black line in **a**, **c**) obtained from various X-probes for a channel flow. These profiles are selectively plotted in a way to demonstrate the effect of varying Δs^+ (**a**, **b**) and l^+ (**c**, **d**). Color coding corresponding to the X-probes is given in Table 1. Dark and light shading represents data from the $Re_\tau \approx 1000$ channel flow experiments and the corresponding synthetic experiments, respectively. Note the vertical shift in profiles for the synthetic experiments

of DNS flow fields to simulate the 'expected' spectra in the small-scale range.

Appendix 4: Database of energy spectra obtained from synthetic experiments

A database of the viscous-scaled premultiplied energy spectra, obtained via synthetic experiments for varying measuring volumes of the X-probes, can be accessed at http://fluids.eng.unimelb.edu.au/. The users can follow the steps summarized in Sect. 6 to correct their X-probe dataset for canonical wall-bounded flows in case of calibration misalignments.

References

Baars W, Squire D, Talluru K, Abbassi M, Hutchins N, Marusic I (2016) Wall-drag measurements of smooth-and rough-wall turbulent boundary layers using a floating element. Exp Fluids 57(5):90

Baidya R (2016) Multi-component velocity measurements in turbulent boundary layers. Ph.D. thesis, University of Melbourne, Department of Mechanical and Manufacturing Engineering

Baidya R, Philip J, Hutchins N, Monty JP, Marusic I (2012) Measurements of streamwise and spanwise fluctuating velocity components in a high Reynolds number turbulent boundary layer. In: Proceedings of 18th Australasian fluid mechanics conference

Baidya R, Philip J, Hutchins N, Monty J, Marusic I (2017) Distance-from-the-wall scaling of turbulent motions in wall-bounded flows. Phys Fluids 29(2):020712

Baidya R, Philip J, Hutchins N, Monty J, Marusic I (2019a) Sensitivity of turbulent stresses in boundary layers to cross-wire probe uncertainties in the geometry and calibration procedure. Meas Sci Technol 30(8):085301

Baidya R, Philip J, Hutchins N, Monty J, Marusic I (2019b) Spatial averaging effects on the streamwise and wall-normal velocity measurements in a wall-bounded turbulence using a cross-wire probe. Meas Sci Technol 30(8):085303

Bradshaw P (2013) An introduction to turbulence and its measurement: thermodynamics and fluid mechanics series. Elsevier, Amsterdam

Browne L, Antonia R, Shah D (1988) Selection of wires and wire spacing for x-wires. Exp Fluids 6(4):286–288

Burattini P (2008) The effect of the x-wire probe resolution in measurements of isotropic turbulence. Meas Sci Technol 19(11):115405

Burattini P, Antonia R (2005) The effect of different x-wire calibration schemes on some turbulence statistics. Exp Fluids 38(1):80–89

Burattini P, Kinet M, Carati D, Knaepen B (2007) Corrections for underresolved scalar measurements in turbulent flows using a DNS database. Exp Fluids 43(1):31–37

Chauhan K, Monkewitz P, Nagib H (2009) Criteria for assessing experiments in zero pressure gradient boundary layers. Fluid Dyn Res 41(2):021404

del Alamo JC, Jiménez J, Zandonade P, Moser RD (2004) Scaling of the energy spectra of turbulent channels. J Fluid Mech 500:135–144

Ganapathisubramani B (2018) Law of the wall for small-scale streamwise turbulence intensity in high-Reynolds-number turbulent boundary layers. Phys Rev Fluids 3(10):104607

Hinze J (1975) Turbulence. McGraw-Hill, New York

Hutchins N, Nickels TB, Marusic I, Chong MS (2009) Hot-wire spatial resolution issues in wall-bounded turbulence. J Fluid Mech 635:103–136

Jørgensen F (1996) The computer-controlled constant-temperature anemometer. Aspects of set-up, probe calibration, data acquisition and data conversion. Meas Sci Technol 7(10):1378

Lee M, Moser RD (2015) Direct numerical simulation of turbulent channel flow up to $Re_\tau \approx 5200$. J Fluid Mech 774:395–415

Lee J, Monty J, Hutchins N et al (2016) Validating under-resolved turbulence intensities for PIV experiments in canonical wall-bounded turbulence. Exp Fluids 57(8):129

Marusic I, Perry A (1995) A wall-wake model for the turbulence structure of boundary layers. Part 2. Further experimental support. J Fluid Mech 298:389–407

Monty J, Stewart J, Williams R, Chong M (2007) Large-scale features in turbulent pipe and channel flows. J Fluid Mech 589:147–156

Monty J, Hutchins N, Ng H, Marusic I, Chong M (2009) A comparison of turbulent pipe, channel and boundary layer flows. J Fluid Mech 632:431–442

Morrill-Winter C, Klewicki J, Baidya R, Marusic I (2015) Temporally optimized spanwise vorticity sensor measurements in turbulent boundary layers. Exp Fluids 56(12):216

Perry A, Lim K, Henbest S (1987) An experimental study of the turbulence structure in smooth-and rough-wall boundary layers. J Fluid Mech 177:437–466

Philip J, Baidya R, Hutchins N, Monty JP, Marusic I (2013) Spatial averaging of streamwise and spanwise velocity measurements in wall-bounded turbulence using v- and ×-probes. Meas Sci Technol 24(11):115302

Sillero JA, Jiménez J, Moser RD (2013) One-point statistics for turbulent wall-bounded flows at Reynolds numbers up to $\delta^+ \approx 2000$. Phys Fluids 25(10):105102

Strohl A, Comte-Bellot G (1973) Aerodynamic effects due to configuration of x-wire anemometers. J Appl Mech 40(3):661–667

Suzuki Y, Kasagi N (1992) Evaluation of hot-wire measurements in wall shear turbulence using a direct numerical simulation database. Exp Therm Fluid Sci 5(1):69–77

Tagawa M, Tsuji T, Nagano Y (1992) Evaluation of x-probe response to wire separation for wall turbulence measurements. Exp Fluids 12(6):413–421

Talluru K, Kulandaivelu V, Hutchins N, Marusic I (2014) A calibration technique to correct sensor drift issues in hot-wire anemometry. Meas Sci Technol 25(10):105304

Tutu N, Chevray R (1975) Cross-wire anemometry in high intensity turbulence. J Fluid Mech 71(4):785–800

Wallace JM, Vukoslavčević PV (2010) Measurement of the velocity gradient tensor in turbulent flows. Annu Rev Fluid Mech 42:157–181

Willmarth WW, Bogar TJ (1977) Survey and new measurements of turbulent structure near the wall. Phys Fluids 20(10):S9–S21

Yavuzkurt S (1984) A guide to uncertainty analysis of hot-wire data. ASME Trans J Fluids Eng 106(2):181–186

Zimmerman S, Morrill-Winter C, Klewicki J (2017) Design and implementation of a hot-wire probe for simultaneous velocity and vorticity vector measurements in boundary layers. Exp Fluids 58(10):148